References

1. André, J.C. [et al.]. 1978. Modeling the 24-hour evolution of the mean and turbulent structures of the planetary boundary layer. *Journal of the Atmospheric Sciences*, **35**, 1861.

2. Andrews, L.C. and Phillips, R.L. 2005. *Laser beam propagation through random media.* 2nd ed. Bellingham, WA: SPIE Press, 2005.

3. Argyle, B. (ed.) 2004. Observing and Measuring Visual Double Stars. *Patrick Moore's Practical Astronomy Series.* London: Springer-Verlag, 2004: 19 & 86.

4. Aristidi, E. [et al.]. 2009. Dome C site testing: surface layer, free atmosphere seeing, and isoplanatic angle statistics. *Astronomy and Astrophysics*, **499**, 955-965.

5. Avila, R., Vernin, J. and Masciadri, E. 1997. Whole atmospheric-turbulence profiling with generalized SCIDAR. *Applied Optics*, **36**(30): 7898-7905.

6. Avila, R. [et al.]. 2008. LOLAS: an optical turbulence profiler in the atmospheric boundary layer with extreme altitude resolution. *Monthly Notices of the Royal Astronomical Society*, **387**(4): 1511-1516.

7. Azouit, M. [et al.].1980. Remote sensing of atmospheric turbulence by means of a fast optical method: a comparison with simultaneous in situ measurements. *Journal of Applied Meteorology*, **19**: 834-838.

8. Azouit, M. and Vernin, J. 2005. Optical turbulence profiling with balloons relevant to astronomy and atmospheric physics. *Publications of the Astronomical Society of the Pacific*, **117**: 536-543.

9. Barletti, R. [et al.].1977. Astronomical site testing with balloon borne radiosondes: results about atmospheric turbulence, solar seeing and stellar scintillation. *Astronomy and Astrophysics*, **54**: 649-659.

10. Beckers, J.M. 1993. On the relation between scintillation and seeing observations of extended objects. *Solar Physics*, **145**(2): 399-402.

11. Beckers, J.M. 2001. A seeing monitor for solar and other extended object observations. *Experimental Astronomy*, **12**: 1–20.

12. Bonner, C.S. [et al.]. 2008. SNODAR: a new instrument to measure the height of the boundary layer on the Antarctic plateau. *Ground-based and Airborne Instrumentation for Astronomy II. Proceedings of the SPIE*, **7014**: 70146I-70146I-7.

13. Bonner, C.S. [et al.]. 2009. SNODAR: an acoustic radar for atmospheric turbulence profiling with 1m resolution. *Acoustics Australia,* **37**(2): 47–51.

14. Bonner, C.S. [et al.]. 2009. SNODAR II: probing the atmospheric boundary layer on the Antarctic plateau. *Optical turbulence: astronomy meets meteorology. Proceedings of the optical turbulence characterization for astronomical applications.* Sardinia, Italy, 15 - 18 September 2008: 264-270.

15. Bonner, C.S. [et al.]. 2010. SNODAR: 2009 performance at Dome A, Antarctica. *Ground-based and Airborne Telescopes III. Proceedings of the SPIE*, **7733**: 77334A-77334A-6.

16. Born, M. and Wolf E. 1999. *Principles of optics: electromagnetic theory of propagation, interference and diffraction of light*. 7th ed. Cambridge: Cambridge University Press, 1999.

17. Breedlove, G. and Jordaan, F. [eds.]. 2000. *Environmental Potential Atlas for South Africa (ENPAT 2000).* Compiled by the Department of Environmental Affairs and Tourism, the University of Pretoria and GIS Business Solutions, July 2000.

18. Bufton, J.L. [et al.]. 1972. Measurements of turbulence profiles in the troposphere. *Journal of the Optical Society of America*, **62**(9): 1068-1070.

19. Cassen, P., Guillot, T. and Quirrenbach, A. 2006. *Extrasolar planet: Saas-Fee Advanced Course 31. The effects of atmospheric turbulence on astronomical observations.* Heidelberg: Springer-Verlag, 2006: 130-142.

20. Chou, S.-H. and Ferguson, M.P. 191. Heat fluxes and roll circulations over the western Gulf Stream during an intense cold-air outbreak. *Boundary-Layer Meteorology*, **55**: 255-281.

21. Combrinck, W.L. and Combrink, A.Z.A. 2004. Proposed new international Space Geodesy Facility for southern Africa. *35th COSPAR Scientific Assembly*, Paris, France, 18-25 July 2004: 270.

22. Committee on the National Requirements for Precision Geodetic Infrastructure; Committee on Seismology and Geodynamics; National Research Council. 2010.

Precise geodetic infrastructure: national requirement s for shared resources. Washington DC: National Academic Press, 2010. Also available at: http://books.nap.edu/catalog.php?record_id= 12954 (accessed 10 July 2011).

23. Combrinck, W.L. [et al.]. 2007. Report on preliminary geotechnical and tropospheric site investigation for a proposed space geodetic observatory near Matjiesfontein in the Great Karoo. *South African Journal of Geology*, **110**(2/3): 225-234.

24. Conan, R. [et al.]. 1999a. Measurement of the optical relevant parameters for high resolution astronomy with the Generalized Seeing Monitor (GSM). *Catching the Perfect Wave: Adaptive Optics and Interferometry in the 21st Century. Proceedings of a symposium held as a part of the 110th Annual Meeting of the ASP.* New Mexico, USA, 28 June-1 July 1998: 27.

25. Conan, R. [et al.]. 1999b. Spatio-temporal analysis of the wave front with the GSM. *Astronomy with Adaptive Optics: present results and future programs. Proceedings of an ESO/OSA topical meeting*. Sonthofen, Germany, 7-11 September 1998, **56**: 133.

26. Coulman, C.E. 1985. Fundamental and applied aspects of astronomical "seeing". *Annual Review of Astronomy and Astrophysics*, **23**: 19-57.

27. Crescenti, G.H. 1997. A look back on two decades of Doppler SODAR comparison studies. *Bulletin of the American Meteorological Society*, **78**(4): 651-673.

28. Dickey, J.O. [et al.]. 1994. Lunar Laser Ranging: a continuing legacy of the Apollo program. *Science*, **265**: 482-490.

29. Dierickx, P. 1992. Optical performance of large ground-based telescopes. *Journal of Modern Optics* **39**(3): 569-588.

30. Echevarría, J. [et al.].1998. Site Testing at Observatorio Astronomico Nacional in San Pedro Mártir. *Revista Mexicana de Astronomía y Astrofísica*, **34**: 47-60.

31. Echevarría, J. 2003. Site Testing at San Pedro Mártir. *San Pedro Mártir: Astronomical Site Evaluation. Revista Mexicana de Astronomía y Astrofísica. Serie de Conferencias*, **19**: 41-43.

32. Egner, S.E. [et al.]. 2006. Beyond conventional G-SCIDAR: the ground-layer in high vertical resolution. *Advances in Adaptive Optics II. Proceedings of the SPIE*, **6272**: 627256.

33. Egner, S.E. and Masciadri, E. 2007. A G-SCIDAR for ground-layer turbulence measurements at high vertical resolution. *Publications of the Astronomical Society of the Pacific*, **119**(862): 1441-1448.

34. Erasmus, D.A. 1986. Meteorological conditions affecting observing quality on Mauna Kea. *Publications of the Astronomical Society of the Pacific* **98**: 254-259.

35. Erasmus, D.A. 1988 & 1996. *Relating seeing quality to meteorological conditions: development of seeing quality forecasts and improvement of site selection procedures.* Available at: http://www.saao.ac.za/~erasmus/overfsee.htm (accessed 6 March 2012).

36. Erasmus, D.A. 2000. Meteorological conditions and astronomical observing quality ('seeing') at candidate sites for the Southern African Large Telescope. *South African Journal of Science* **96**: 1-8.

37. Esau, I. 2004. Simulation of Ekman boundary layers by large eddy model with dynamic mixed subfilter closure. *Environmental Fluid Mechanics*, **4**(3): 273-303.

38. Fried, D.L. 1965. Statistics of a geometric representation of wave front distortion. *Journal of the Optical Society of America* **55**(11): 1427-1435.

39. Fried, D.L. 1966. Optical resolution through a randomly inhomogeneous medium for very long and very short exposures. *Journal of the Optical Society of America* **56**(10): 1372-1379.

40. Fuchs, A., Tallon, M. and Vernin, J. 1998. Focusing on a turbulent layer: principle of the "Generalized SCIDAR". *Publications of the Astronomical Society of the Pacific*, **110**(743): 86-91.

41. Fuensalida, J.J. [et al.]. 2004. An automatically controlled SCIDAR instrument for Roque de los Muchachos Observatory. *Second Backaskog Workshop on Extremely Large Telescopes. Proceedings of the SPIE*, **5382**: 643-647.

42. Garrat, J.R. 1992. *The atmospheric boundary layer. Cambridge atmospheric and space science series.* Cambridge: Cambridge University Press, 1992.

43. Grant, A.L.M. 1992. The structure of turbulence in the near-neutral atmospheric boundary layer. *Journal of the Atmospheric Sciences* **49**: 226-239.

44. Howell, S.B. 2006. *Handbook of CCD Astronomy*. Cambridge: Cambridge University Press, 2006.

45. Kolmogorov, A.N. 1941. The local structure of turbulence in incompressible viscous fluid for very large Reynolds' numbers. *Comptes rendes (Doklady) de l'Academie des Sciences de l'USSR* **30**: 301-305.

46. Kornilov, V. [et al.]. 2003. MASS: a monitor of the vertical turbulence distribution. *Adaptive Optical System Technologies II. Proceedings of the SPIE*, **4839**: 837-845.

47. Kornilov, V. [et al.]. 2007. Combined MASS-DIMM instruments for atmospheric turbulence studies. *Monthly Notices of the Royal Astronomical Society*, **382**: 1268-1278.

48. Kruger, A. C. 2004. *Climate of South Africa. Climate Regions. WS45.* South African Weather Service. Pretoria. South Africa.

49. Lawrence, J.S. [et al.]. 2007. Characterisation of the Dome C atmospheric boundary layer turbulence with a non-Doppler acoustic radar. *EAS Publications Series*, **25**: 31-34.

50. Léna, P. 1986. *Observational astrophysics*. Berlin: Springer-Verlag, 1986.

51. Longair, M.S. 1992. *High energy astrophysics: particles, photons and their detection.* 2nd ed. New York: Cambridge University Press, 1992.

52. Martin, F. [et al.]. 1994. GSM: a Grating Scale Monitor for atmospheric turbulence measurements: I. The instrument and first results of angle of arrival measurements. *Astronomy and Astrophysics Supplement Series*, **108**: 173-180.

53. Martinez, P. & Klotz, A. 1998. *A Practical Guide to CCD Astronomy*. Cambridge: Cambridge University Press, 1998.

54. Mobberley, M. 1998. *Astronomical Equipment for Amateurs*. London: Springer-Verlag, 1998.

55. Moeng, C.-H. and Sullivan, P.P. 1994. A comparison of shear- and buoyancy-driven planetary boundary layer flows. *Journal of the Atmospheric Sciences*, **51**(7): 999-1022.

56. Moore, A. [et al.]. 2006. Ground-layer turbulence profiling using a lunar SHABAR. *Ground-based and Airborne Telescopes. Proceedings of the SPIE*, **6269**: 62695U.

57. Napier-Munn, T. 2008. A mathematical model to predict the resolution of double stars by amateurs and their telescopes. *Journal of Double Star Observations* **4**(4): 156-163.

58. Nappo, C.J. 1991. Sporadic breakdowns of stability in the PBL over simple and complex terrain. *Boundary-Layer Meteorology* **54**(1-2): 69-87.

59. Obukhov, A.M. 1941. On the Distribution of Energy in the Spectrum of Turbulent Flow. *Doklady Akad. Nauk SSSR* **32**(1): 19-24.

60. Pope, S.B. 2000. *Turbulent flows*. Cambridge: Cambridge University Press, 2000.

61. Osborn, J. [et al.]. 2010. Profiling the surface layer of optical turbulence with SLODAR. *Monthly Notices of the Royal Astronomical Society*, **406**: 1405-1408.

62. Robert, C. [et al.]. 2009. C_n^2 profile from Shack-Hartmann data: first steps for CO-SLIDAR data processing. *Optical turbulence: astronomy meets meteorology. Proceedings of the optical turbulence characterization for astronomical applications*. Sardinia, Italy, 15 - 18 September 2008: 74-81.

63. Robert, C. [et al.]. 2011. *C_n^2 profile from Shack-Hartmann data with CO-SLIDAR data processing*. eprint arXiv:1101.3924. Available at: http://arxiv.org/abs/1101.3924 (accessed 10 October 2012).

64. Rocca, A, Roddier, F. and Vernin, J. 1974. Detection of atmospheric turbulent layers by spatiotemporal and spatioangular correlation measurements of stellar-light scintillation. *Journal of the Optical Society of America*, **64**(7): 1000-1004.

65. Roddier, F. 1981. *The effects of atmospheric turbulence in optical astronomy*. Progress in Optics. Amsterdam: North Holland Publishing, **19**: 283-376.

66. Roggeman, M.C. and Welsh, B. 1996. *Imaging through turbulence*. Boca Raton: CRC Press, 1996.

67. Sánchez, L.J. [et al.]. 2003. San Pedro Mártir: Astronomical Site Evaluation. *Astronomical Site Evaluation. Revista Mexicana de Astronomía y Astrofísica. Serie de Conferencias*, **19**: 23-30.

68. Sarazin, M. and Roddier, F. 1990. The ESO differential image motion monitor. *Astronomy and Astrophysics*, **227**: 294-300.

69. Sliepen, G. [et al.]. 2010. Seeing measurements with autonomous, short-baseline shadow band rangers. *Ground-based and Airborne Telescopes III. Proceedings of the SPIE*, **7733**: 77334L-77334L-11.

70. Starizona. 2000. *Starizona's Guide to CCD Imaging*. Available at: http://starizona.com/acb/ ccd/ccd.aspx (accessed 7 May 2012).

71. Stull, R.B. 1988. *An introduction to boundary layer meteorology*. Dordrecht: Kluwer Academic Publishers, 1988.

72. Tatarski, V.I. 1961. *Wave propagation in a turbulent medium*. New York: Dover Publications, 1961.

73. *The Sixth Catalog of Orbits of Visual Binary Stars*. 2006. 6th ed. , Washington, DC: U.S. Naval Observatory, 2006. Available at: http://ad.usno.navy.mil/wds/orb6/orb6ephem.html (accessed 15 April 2012).

74. Tokovinin, A. [et al.]. 2003. Restoration of turbulence profile from scintillation indices. *Monthly Notices for the Royal Astronomical Society*, **343**: 891-899.

75. Tokovinin, A. 2007. Turbulence profiles from the scintillation of stars, planets, and moon. *Workshop on Astronomical Site Evaluation. Revista Mexicana de Astronomía y Astrofísica. Serie de Conferencias*, **31**: 61-70.

76. Tokovinin, A., Bustos, E. and Berdja, A. 2010. Near-ground turbulence profiles from lunar scintillometer. *Monthly Notice of the Royal Astronomical Society*, **404**: 1186-1196.

77. Travouillon, T. 2004. *Optical turbulence on the Antarctic plateau*. September, 2004 [PhD thesis].

78. Trinquet, H. and Vernin, J. 2006. A model to forecast seeing and estimate C_N^2 profiles from meteorological data. *Publications of the Astronomical Society of the Pacific* **118**, 756-764.

79. Trinquet, H. [et al.]. 2008. Nighttime Optical Turbulence Vertical Structure above Dome C in Antarctica. *Publications of the Astronomical Society of the Pacific*, **120**: 203-211.

80. Tubbs, R.N. 2003. *Lucky exposures: diffraction limited astronomical imaging through the atmosphere*. September, 2003 [PhD thesis].

81. Védrenne, N. [et al.]. 2007. C_n^2 profile measurement from Shack-Hartmann data. *Optics Letters*, **32**(18): 2659-2661.

82. Vernin, J. and Muñoz-Tuñón, C. 1992. Optical seeing at La Palma Observatory, I. General guidelines and preliminary results at the Nordic Optical Telescope. *Astronomy & Astrophysics* **257**: 811-816.

83. Vernin, J. and Muñoz-Tuñón, C. 1995. Measuring astronomical seeing: the DA/IAC DIMM. *Publications of the Astronomical Society of the Pacific*, **107**: 265-272.

84. Vernin, J. and Roddier, F. 1973. Experimental determination of two-dimensional spatiotemporal power spectra of stellar light scintillation. Evidence for a multilayer structure of the air turbulence in the upper troposphere. Journal *of the Optical Society of America*, **63**(3): 270-273.

85. Wargau, W.F. 1994. Comparing seeing measurements at SAAO/Sutherland, Gamsberg/Namibia and ESO/La Silla. *Monthly Notices of the Astronomical Society of Southern Africa* **53** (9 & 10): 88-89.

86. Wilson, R.W. 2002. SLODAR: measuring optical turbulence altitude with a Shack-Hartmann wavefront sensor. *Monthly Notice of the Royal Astronomical Society*, **337**(1): 103-108.

87. Wilson,R.W., Butterley, T. and Sarazin, M. 2009. The Durham/ESO SLODAR optical turbulence profiler. *Monthly Notices of the Royal Astronomical Society*, **399**(4): 2129-2138.

88. Wilson, R.W., Butterley, T. and Osborn, J. 2009. Slodar Turbulence Monitors. *Optical turbulence: astronomy meets meteorology. Proceedings of the optical turbulence characterization for astronomical applications*. Sardinia, Italy, 15 - 18 September 2008: 50-57.

89. Wodaski, R. 2002. *The New CCD Astronomy.* Washington: New Astronomy Press, 2002.

90. Ziad, A., [et al.]. 2000. From the Grating Scale Monitor to the Generalized Seeing Monitor. *Applied Optics*, **39**(30): 5415-5425.

91. Ziad, A. [et al.]. 2010. Monitoring of the atmospheric turbulence profiles for the specification of ELT's adaptive optics systems. *Ground-based and Airborne Telescopes III. Proceedings of the SPIE*, **7733**: 77334J-77334J-7.

Appendix A1

Potential sites for locating a new fundamental space geodetic observatory are briefly described referring to factors influencing atmospheric turbulence / astronomical seeing at a site, such as climate, topography and vegetation with reference to Breedlove & Jordaan (2000) and Kruger (2004) –
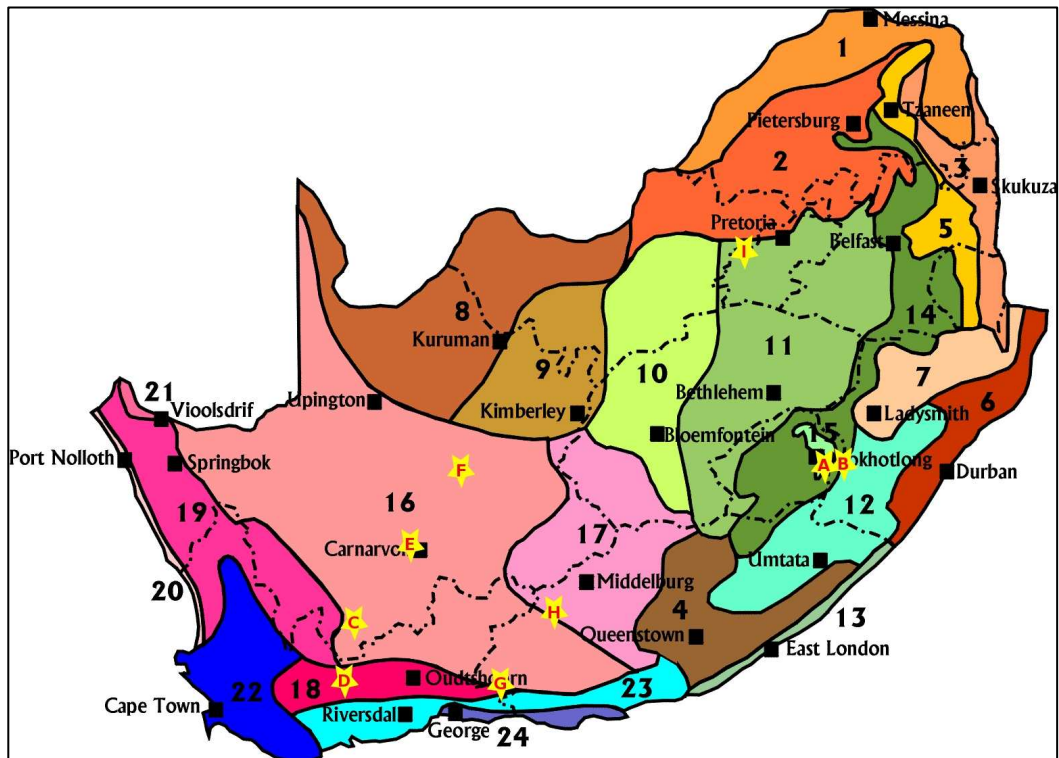

Figure A1.1. Potential sites for a new fundamental space geodetic observatory (and the climatic regions of South Africa in which they are located) (source: Kruger, 2004).

1 Northern Arid Bushveld 2 Central Bushveld 3 Lowveld Bushveld 4 South-Eastern Thornveld 5 Lowveld Mountain Bushveld 6 Eastern Coastal Bushveld 7 KwaZulu-Natal Central Bushveld 8 Kalahari Bushveld 9 Kalaharu Hardveld Bushveld 10 Dry Highveld Grassland 11 Moist Highveld Grassland 12 Eastern Grassland 13 South-Eastern Coast Grassland 14 Eastern Mountain Grassland 15 Alpine Heathland 16 Great and Upper Karoo 17 Eastern Karoo 18 Little Karoo 19 Western Karoo 20 West Coast 21 North-Western Desert 22 Southern Cape Forest 23 South-Western Cape 24 Southern Cape.

- Lesotho [A]: The first site identified and investigated was in Lesotho at 3300 m above sea level. The initial costs for infrastructure were far too high however (Combrinck & Combrink, 2004 and Combrinck *et al*., 2007).

- Underbergh/Shaleburn [B]: Since the Lesotho site is not viable, an area in and around Underbergh has come under investigation. Shaleburn weather station is located in KwaZulu-Natal, ~ 15 km west of Underbergh, at the foot of the Drakensberg. It is

surrounded by the mountains of the Great Escarpment with elevations of between 1500 and 3000 m. It lies on the Eastern Plateau Slope at an elevation of 1609 m. It is in an area of lowlands with high and low mountains and strongly undulating irregular land. Grassland and cultivated land covers the area. It lies on the border of the alpine heathland and eastern grassland climate region. Rainfall is high and occurs mainly during the summer, peaking between December and February.

- Sutherland [C]: The South African Astronomical Observatory (SAAO) site at Sutherland was also considered. Sutherland is located in the southern Northern Cape. The site is located on the interior plain at an elevation of ~ 1760 m. Mountains and lowlands with shrubland predominate. It falls in the Great and Upper Karoo climate region of South Africa. It is a dry and extreme climate. Rainfall is autumnal. In winter, temperatures are very low and the wind comes from the north. In summer, temperatures are high and the wind comes from the south-west. Concerns were raised about the laser (from the laser ranger) causing too much light pollution (Combrinck & Combrink, 2004 and Combrinck *et al*., 2007). Astronomical seeing is determined by the Differential Image Motion Monitoring (DIMM) technique at SAAO. It would be ideal to compare seeing monitor and DIMM measurements at this site. Future collaboration with SAAO is to be continued.

- Matjiesfontein [D]: A valley just 4 km south of Matjiesfontein was identified next. The Matjiesfontein Village Educational Trust indicated that they will donate this piece of land for the use of a space geodetic observatory. Matjiesfontein is located in the Western Cape, ~ 100 km south of Sutherland, in close proximity to SAAO facilities. The site is at elevations between 800 and 1500 m and forms part of the Cape Fold region (Witteberge). It is surrounded by low mountains and lowlands with parallel hills. Land cover consists of shrubland and fynbos. It falls in the Little Karoo climate region of South Africa with low autumnal rainfall. The site provides clear skies (low cloud cover and water vapour content) and infrastructure (close to N1 and railway station, gravel road to site, overhead high voltage line ~ 1 km from site, new water source nearby, small local community) and is accessible. It is located in a small depression shielding it from RFI. The Council for Geoscience conducted geophysical and geotechnical site surveys, which included a magnetic, electromagnetic and seismic

refraction survey. The site meets criteria for site stability. Preliminary astronomical seeing measurements indicated that seeing at the site was comparable to that of Sutherland. The technique employed a small telescope to resolve features on the Moon with known angular separation. This delivered periods of good seeing (1-2 arc-sec) (Combrinck *et al*., 2007).

Figure A1.2. Panoramic view – Matjiesfontein site (courtesy: Roelf Botha).

Figure A1.3. From left to right: Matjiesfontein site – looking north towards proposed LLR location on ridge; on-site Davis Vantage Pro2 Automatic Weather Station (AWS); looking southeast from the LLR ridge down into the valley.

- Klerefontein [E]: The most recently proposed location is the Karoo Array Telescope (KAT) / Square Kilometre Array (SKA) base-station at Klerefontein, which lies 10 km west of Carnarvon in the Northern Cape and ~ 190 km northeast of Sutherland. The site is at an elevation of ~ 1300 m. It forms part of the central interior plain with lowlands and parallel hills. Land cover consists of shrubland. It falls in the Great and Upper Karoo climate region. This site offers the necessary infrastructure (roads, electrical mains power, high-speed fibre-optic link, support facilities, accommodation) without any additional expense to HartRAO. Locating a HartRAO outstation at the KAT/SKA base-station should also promote synergy with the MeerKAT project. The Space Geodesy programme has already been tasked with installing a weather station and GNSS receiver at the site in support of observations made by the C-Band All Sky Survey (C-BASS) telescope located there. Klerefontein is situated in the Astronomy Geographic Advantage Protection (AGAP) zone, which precludes locating an S/LLR

3

with aircraft detection by radar at the site. It would therefore be necessary to furbish any S/LLR system intended for Klerefontein with optical aircraft detection. A Russian SLR system, which HartRAO has been asked to host, uses optical aircraft tracking, and Klerefontein would therefore be an ideal location to place such a system.

- Prieska [F]: Hilly areas to the north and south of Prieska came under consideration due to the extremely low cloud cover at this locality. Prieska is located in the Northern Cape ~ 160 km northeast of Klerefontein. It lies on the interior pre-Karoo surface with hills and slightly irregular plains dominating the landscape. The elevation varies between ~ 1200 and 1400 m. Land cover consists of shrubland thicket and bushland. Similar to Sutherland and Klerefontein, it falls in the Great and Upper Karoo climate region.

- Willowmore [G]: Hilly and mountainous areas encircle Willowmore, which is located in the Eastern Cape ~ 270 km east of Matjiesfontein. The elevation varies between ~ 800 and 1500 m. It forms part of the Cape Fold region with both high and low mountains as well as lowlands with parallel hills occurring. Shrubland and fynbos make up the degraded land cover. The area is ~ 80 km from the Indian Ocean where the climate regions of the Little, Great and Upper Karoo as well as South Western Cape meet.

- Graaff-Reinet [H]: This Eastern Cape town is located ~ 160 km northeast of Willowmore. It forms part of the mountains of the Great Escarpment. A mountainous region, starting to the east of Graaff-Reinet and sweeping through an arc to the southwest, surrounds the town. Shrubland, fynbos and grassland provide degraded land cover. Climate regions of the Great and Upper Karoo as well as Eastern Karoo meet here. The Eastern Karoo is a wetter region than the Great and Upper Karoo and the late-summer to autumn rainfall season peaks from February to March.

In comparing the above sites for water vapour, rainfall and cloud cover (data from http://disc.sci.gsfc.nasa.gov/AIRS as well as www.weathersa.co.za), Shaleburn and Sutherland have the least amount of water vapour, Matjiesfontein and Klerefontein the lowest annual rainfall, while Klerefontein and Prieska have the least amount of cloud cover.

HartRAO [I] will be employed as reference and test site. HartRAO is located ~ 50 km northwest of Johannesburg, just inside Gauteng's border with Northwest Province. HartRAO lies in the central highlands at an elevation of ~ 1380 m with highly dissected and undulating parallel hills as well as lowlands surrounding it. Land cover consists of thicket and bushland, woodland as well as grassland. The regional climate is moist highveld grassland bordering on central bushveld. Rainfall maximum occurs during December and January. The 1-m OCA telescope will be refurbished at HartRAO in a movable structure that is being built on-site for housing the entire S/LLR system in the end. On completion, the S/LLR system will be relocated to the chosen site for the new fundamental space geodetic station.

Appendix A2

An Octave program, 'plot_CN2_notlog_8.m' below, was written and used to calculate $C_N{}^2(h)$ from the $C_T{}^2(h)$ profile as well as temperature $T(h)$ and pressure $P(h)$ profiles. The $C_T{}^2$ parameter was calculated from rates of temperature variance dissipation ε_θ and turbulence kinetic energy dissipation $\varepsilon^{-\frac{1}{3}}$ by calling the Octave program, 'dissipationLES64.m' also given below, provided by Dr Esau from NERSC.

plot_CN2_notlog_8.m

```
%
% calculate CN2 from Gladstone law (CT2) making use of relative humidity (RH) and
gradtheta
clear;
unorgb=[1 1 1];
% temperature at Matjies [K] (=10 C)
Tbase=283;
% pressure at Matjies in Pa (convert back to hPa/mbar before using in Gladstone's
equation)
Pbase=90500;
% relative humidity (ratio of actual mixing ratio,r, to saturation mixing ratio, xs)
RH=70;
% constant? in Classius Clapeyron equation
eps=0.622
% heat of vaporisation of water (latent heat: water vapour) [J/kg]
Hv=2.257e6
% universal gas constant [J/(kmol.K)]
R=8310
% Specific gas constant [J/(kg.K)]: dry air - sd, water vapour - sw
Rsd=287.052;
Rsw=462;
% Specific heat [J/(kg.K)]: air - a, water vapour - w
%Cpa=1004;
Cpd=1004;
Cpw=1840;
%gravitational acceleration [m/s2]
g=9.8076;
% pressure constant in Gladstone relation [hPa]=[100 Pa]
Pg=80e-6;
% wavelength of green laser light [m]
lamda=532e-9;
%% load database64
load -mat DATABASE64_16hr_final.bin;
load -mat DATABASE64_16hr_final_3D.bin;
% select only tst cases
```

```matlab
ind_tst=[indexdb.tst_begin:indexdb.tst_finish]; nn_total=numel(ind_tst);
q=squeeze(db(ind_tst)); q3=squeeze(d3(ind_tst));
clear db d3;
% calculate spectral dissipations1
for ii=1:nn_total;
    dq(ii)=dissipationLES64(q(ii),q3(ii),4,20,11,2);
end;
%
% initialize total CN2 for summing and calculating q1
CN2total=0;
%initialize q's for summing
q_1total=0;
q_2total=0;
q_3total=0;
q_4total=0;
q_5total=0;
% surface Monin-Obukhov length scale [m] (Ls-von Karman const)
%Ls=18.5885;
psi=1-(2.5*(q(8).z(2)/q(8).Ls(32)));
% surface temperature, T1 [K] (ts-theta star; kappa-temperature scale [K]; surface
roughness [m])
T(1)=Tbase-(q(8).ts(32)/q(8).kappa)*((log(q(8).z(2)/(2*q(8).z0)))-psi);
% surface pressure
P(1)=Pbase;
% CT2 at surface
CT2(1)=1.6*(dq(8).mt_mean_rdissEt)(1).*(dq(8).mt_mean_rdissEk.^(-1/3))(1);
% CN2 at surface
CN2(1)=((Pg*(P(1)/100)/((T(1))^2))^2)*CT2(1);
%
for k=1:63;
% saturated vapour pressure (depends on T (not a constant T0) so therefore variable?)
es(k)=611*exp((eps*Hv/Rsd)*((1/273)-(1/(T(k)))));
% saturation mixing ratio (depends on es (not constant T0) and P (not constant P0) so
therefore also variable?)
xs(k)=eps*(es(k))/(P(k));
% actual mixing ratio from RH and xs (saturated mixing ratio)
r(k)=(RH/100)*(xs(k));
% adiabatic rate
gamma(k)=g*(1+((Hv*(r(k)))/(Rsd*(T(k)))))/(Cpd+((Hv^2)*(r(k))*eps/(Rsd*((T(k))^2)))
);
% temperature profile
T(k+1)=T(k)+(((q(8).gradT(k,32))+gamma(k))*(dq(8).z(k)-dq(8).z(k+1)));
% pressure profile
P(k+1)=P(k)-g*(dq(8).z(k+1)-dq(8).z(k))*(P(k)/(Rsd*T(k)));
%CT2 from dissipations
CT2(k+1)=1.6*(dq(8).mt_mean_rdissEt)(k+1).*(dq(8).mt_mean_rdissEk.^(-1/3))(k+1);
%CN2 profile from Gladstone's relation
CN2(k+1)=((Pg*(P(k+1)/100)/((T(k+1))^2))^2)*CT2(k+1);
CN2total=CN2total+CN2(k+1);
% q's
```

```matlab
q_1(k)=CN2(k+1);
q_2(k)=q_1(k)*((dq(8).z(k))^(5/3));
q_3(k)=q_1(k)*((dq(8).z(k))^(5/6));
q_4(k)=q_1(k)*((q(8).absU(k,32))^(5/3));
q_5(k)=q(8).uu(k,32)/q(8).Nbv(k,32);
% q's summed
q_1total=q_1total+q_1(k);
q_2total=q_2total+q_2(k);
q_3total=q_3total+q_3(k);
q_4total=q_4total+q_4(k);
q_5total=q_5total+q_5(k);
end;
% Integrals
I1=q_1total;
I2=q_2total;
I3=q_3total;
I4=q_4total;
I5=real(q_5total);
% Seeing parameters
r0=(0.423*((2*pi/lamda)^2)* I1)^(-3/5);     % Fried parameter [m]
epsilonFWHM=0.98*lamda/r0;              % Seeing (FWHM) [radian]
hAO=(I2/I1)^(3/5);                % Seeing layer [m]
thetaAO=0.31*r0/hAO;                 % isoplanatic angle [radian]
sigmaI_sq=19.12*(lamda^(-7/6))*I3;       % scintillation rate [%]
vAO=(I4/I1)^(3/5);                % wave front parameter [m/s]
tauAO=0.31*r0/vAO;                 % coherent wave front time [s]
fG=1/tauAO;                 % Greenwood frequency
epsilonTOT=5.41*(lamda^(-1/5))*((I1)^(3/5)); % median seeing in whole atmosphere
L0=(I5/I1)^(-3)                 % Special coherence outer scale (Nbv
                    - Brunt-Vaisala frequency [1/s],
                     % uu  - total <U'U'> [m2/s2])
figure;
% P profile
%plot((P(1:end)/100),dq(1).z(1:end),'g-','LineWidth',2); hold on;
%xlabel('Pressure [hPa]'); ylabel('z [m]');
%grid;
%print('-dpng','P1_CN2_from_CT2_humidity_gradtheta_test_1.png');
%print('-depsc','P1_CN2_from_CT2_humidity_gradtheta_test_1.eps');
%semilogx(q(1).gradT(:,32), dq(1).z(1:end),'m-','LineWidth',2); hold on;
%xlabel('d{\theta}/dz'); ylabel('z [m]');
% T profile
%plot(T(1:end),dq(1).z(1:end),'c-','LineWidth',2); hold on;
%xlabel('Temperature [K]'); ylabel('z [m]');
% CN2 profile
plot(CN2(1:end),dq(1).z(1:end),'r-','LineWidth',2); hold on;
% CT2 profile - dissipations
%semilogx(CT2(1:end),dq(1).z(1:end),'b-','LineWidth',2); hold on;
xlabel('C_{\fontsize{10}_N}^{2}'); ylabel('z [m]');
%semilogx(dq(1).mt_mean_rdissEt,dq(1).z,'g-','LineWidth',2); hold on;
%semilogx(dq(1).mt_mean_rdissEk,dq(1).z,'c-','LineWidth',2); hold on;
```

```
print('-dpng','CN2_notlog_8.png');
print('-depsc','CN2_notlog_8.eps');
```

dissipationLES64.m
```
function d=dissipationLES64(q,q3,nv,dbin,navr,tint);
% d=dissipationLES64(q,q3,nv,dbin,navr,tint);
% calculate the structure with dissipation and related characteristics
% from LESNIC database 64
% dbin - number of averaging intervals for spectra approximation
% navr - number of bins in Kolmogorov subrange of scale
% tint - number of samples in time averaging
%% Set up common data
d.file_name=q.fname;
d.nx=q.ndim(1); d.ny=q.ndim(2); d.nz=q.ndim(3); d.nv=q.ndim(5); d.nt=q.ndim(4);
d.tint=tint;
d.lx=q3.ldim(1); d.ly=q3.ldim(1); d.fac=q3.ldim(1)/q3.ndim(1);
d.dbin=dbin; d.navr=navr;
nx=d.nx; nz=d.nz;
b=9.81/300;
nt=numel([q.u(1,:)]); TT=[nt-tint+1:nt];
d.z=q.z;
d.mt_u=squeeze(mean(q.u(:,TT),2));                      d.mt_v=squeeze(mean(q.v(:,TT),2));
d.mt_absU=abs(d.mt_u+i*d.mt_v);
d.mt_gradU=gradient(d.mt_absU,d.z');
d.mt_gradu=gradient(d.mt_u,d.z'); d.mt_gradv=gradient(d.mt_v,d.z');
d.mt_t13(1:nz-1)=squeeze(mean(q.uw(2:nz,TT),2));
d.mt_t23(1:nz-1)=squeeze(mean(q.vw(2:nz,TT),2));
d.mt_t13(nz)=d.mt_t13(nz-1); d.mt_t23(nz)=d.mt_t23(nz-1);
d.mt_us=sqrt(abs(d.mt_t13+i*d.mt_t23));
d.mt_mean_rdissEk=max(0,abs([d.mt_t13]'.*d.mt_gradu+i*([d.mt_t23]'.*d.mt_gradv)));
if (nv>3);  % calculate potential energy dissipation
   d.mt_th=squeeze(mean(q.absT(:,TT),2));
   d.mt_gradT=gradient(d.mt_th,d.z');
   d.mt_rN=sqrt(b*d.mt_gradT);
   d.mt_wt(1:nz-1)=squeeze(mean(q.wt(2:nz,TT),2));
   d.mt_wt(nz)=d.mt_wt(nz-1);
   d.mt_mean_rdissEk=max(1e-12,d.mt_mean_rdissEk+b*[d.mt_wt]');
   d.mt_mean_rdissEt=max(1e-12,-[d.mt_wt]'.*d.mt_gradT);
   d.mt_mean_rRig=b*d.mt_gradT./d.mt_gradU.^2;
%                                                          d.mt_mean_rRifd=-
b*d.mt_wt./abs(d.mt_t13.*[d.mt_gradu]'+i*(d.mt_t23.*[d.mt_gradv]'));
   d.mt_mean_rRifd=-
b*d.mt_wt./(abs(d.mt_t13+i*d.mt_t23).*abs([d.mt_gradu]'+i*[d.mt_gradv]'));
   d.mt_mean_rN=d.mt_rN;
   d.mt_mean_rL=-sqrt(abs(d.mt_t13+i*d.mt_t23)).^3./(b*d.mt_wt);
   d.mt_mean_rdissEp=d.mt_mean_rdissEt.*(b./d.mt_mean_rN).^2;
   d.mt_mean_rRif=d.mt_mean_rdissEp./(d.mt_mean_rdissEk+d.mt_mean_rdissEp);
else
   d.mt_th=d.mt_u*nan; d.mt_N=d.mt_th; d.mt_gradT=d.mt_th;
```

```
    d.mt_wt=d.mt_t13*nan; d.mt_mean_rL=d.mt_wt;
    d.mt_mean_rRig=d.mt_mean_rdissEk; d.mt_mean_rRifd=d.mt_mean_rdissEk;
    d.mt_mean_rdissEt=d.mt_mean_rRig; d.mt_mean_rN=d.mt_mean_rRig;
    d.mt_mean_rdissEp=d.mt_mean_rdissEt;
    d.mt_mean_rRif=d.mt_mean_rdissEp;
end;
% find the turbulent PBL depth
ind=min(nx,min(find([d.mt_us].^2<0.05*[d.mt_us(1)].^2)+1));
d.mt_rHtau05=d.z(ind); d.mt_iHtau05=ind;
%% Second step: spectral dissipation from Kolmogorov interval of scales
disp(['Read ' d.file_name]);
Z1=[floor(1/5*d.mt_iHtau05):round(2/3*d.mt_iHtau05)];
x(:,:,:,1)=[q3.u3d];
x(:,:,:,2)=[q3.v3d];
x(:,:,:,3)=[q3.w3d];
x(:,:,:,4)=[q3.t3d];
ny=numel(squeeze(x(1,:,1,1))); d.ny_used=ny;
NFFT = 2^nextpow2(nx); % Next power of 2 from length of y
K = d.fac/2*linspace(0,1,NFFT/2);
Kx = [0:1:NFFT/2-1]; d.Kx=Kx; d.nKx=numel(Kx); nKx=d.nKx;
% obtain dissipation on each level
% interpolate the vertical velocity on U levels
for iz=2:nz; x(:,:,iz-1,3)=0.5*(x(:,:,iz,3)+x(:,:,iz-1,3)); end;
% calculate anomalies
xm=squeeze(mean(mean(x,2),1));   for  iv=1:nv;   for  iz=1:nz;   xa(:,:,iz,iv)=x(:,:,iz,iv)-
xm(iz,iv); end; end;
% calculate turbulent energy and velocity variations
e=squeeze(0.5*(xa(:,:,:,1).^2+xa(:,:,:,2).^2+xa(:,:,:,3).^2));
sex=squeeze(2*abs(fft(e,NFFT,1)/nx)); % absolute values of the energy spectra in x
(streamwise) direction
disp('Calculate TKE dissipation');
for iz=1:nz;
   icmp=floor(iz/nz*100); if (mod(icmp,20)==0); disp(['Completed ' num2str(icmp) '%']);
end;
   for iy=1:ny; disx(:,iy,iz)=(sex(Kx+1,iy,iz)'.*K.^(5/3)).^(3/2); end;
   d.last_u(iz)=squeeze(mean(mean(x(:,:,iz,1),2),1));
   d.last_v(iz)=squeeze(mean(mean(x(:,:,iz,2),2),1));
   d.last_U(iz)=squeeze(mean(mean(abs(x(:,:,iz,1)+i*x(:,:,iz,2)),2),1));
   d.last_t13(iz)=squeeze(mean(mean(xa(:,:,iz,1).*xa(:,:,iz,3),2),1));
   d.last_t23(iz)=squeeze(mean(mean(xa(:,:,iz,2).*xa(:,:,iz,3),2),1));
   d.last_Ek(iz)=squeeze(mean(mean(e(:,:,iz),2),1));
end;
d.last_gradu=gradient(d.last_u,d.z');
d.last_gradv=gradient(d.last_v,d.z');
d.last_gradU=gradient(d.last_U,d.z');
d.last_us=sqrt(abs(d.last_t13+i*d.last_t23));
[d.kx,d.dissEk,d.last_dissEk,d.factor_dissEk]=aggregation(nKx,dbin,navr,disx,d.mt_mean
_rdissEk,Z1);
%
if (nv>3);
```

% calculate temperature fluctuations spectra along x

```
   tt=0.5*xa(:,:,:,4).^2;
   stx=squeeze(2*abs(fft(tt,NFFT,1)/nx)); % absolute values of the energy spectra in x
(streamwise) direction
   disp('Calculate TPE dissipation');
   for iz=1:nz;
      icmp=floor(iz/nz*100); if (mod(icmp,20)==0); disp(['Completed ' num2str(icmp)
'%']); end;
      for iy=1:ny; dtx(:,iy,iz)=(stx(Kx+1,iy,iz).*(disx(:,iy,iz)).^(1/3))'.*K.^(5/3); end;
      d.last_wt(iz)=squeeze(mean(mean(xa(:,:,iz,4).*xa(:,:,iz,3),2),1));
      d.last_th(iz)=squeeze(mean(mean(x(:,:,iz,4),2),1));
      d.last_Et(iz)=squeeze(mean(mean(tt(:,:,iz),2),1));
   end;
   d.last_gradT=gradient(d.last_th,d.z');
   d.last_N=sqrt(b*d.last_gradT+1e-6);
   d.last_Ep=d.last_Et.*(b./d.last_N).^2;
   d.last_L=-abs(d.last_t13+i*d.last_t23).^(3/2)./(b*d.last_wt+1e-6);

[d.kx,d.dissEt,d.last_dissEt,d.factor_dissEt]=aggregation(nKx,dbin,navr,dtx,d.mt_mean_rd
issEt,Z1);
% calculate own Rig
   d.last_Rig=[d.last_N].^2./[d.last_gradU].^2;
   d.last_Rifd=-b*d.last_wt./abs(d.last_t13.*d.last_gradu+i*(d.last_t23.*d.last_gradv));
   d.last_dissEp=d.last_dissEt.*(b./[d.last_N]).^2;
   d.last_Rif=d.last_dissEp./(d.last_dissEk+d.last_dissEp);
else
   d.factor_dissEt=nan; % const
   d.dissEt=d.dissEk.*d.factor_dissEt;
   d.last_dissEt=d.last_dissEk.*d.factor_dissEt; d.last_dissEp=d.last_dissEk
   d.last_th=d.last_U*nan; d.last_gradT=d.last_th; d.last_N=d.last_th; d.last_wt=d.last_th;
   d.last_Et=d.last_th; d.last_Ep=d.last_th; d.last_L=d.last_th;
   d.last_Rig=d.last_dissEt; d.last_Rifd=d.last_dissEt;
end;
%% Final step: functions
function [k,x,mx,factor]=aggregation(nk,dbin,navr,s,r,Z);
% local function for aggregation of the results
%
Bx=floor(linspace(1,nk,dbin));
for ii=1:dbin-1;
   x1(ii,:,:)=squeeze(mean(s(Bx(ii):Bx(ii+1),:,:),1));
   k(ii)=0.5*(Bx(ii)+Bx(ii+1));
end;
x1(ii+1,:,:)=x1(ii,:,:); k(ii+1)=k(ii);
x=squeeze(mean(x1,2)); avr=min(navr,dbin-2);
mx=squeeze(mean(x(dbin-avr-1:dbin-1,:),1));
factor=mean(r(Z))/mean(mx(Z)); % const
x=x*factor; mx=mx.*factor;
```

Appendix A3

Definition of CCD camera terms:

Bit depth / Analogue to Digital (A/D) resolution - of 16 bits implies that, during analogue-to-digital conversion (ADC), the CCD camera is capable of converting the analogue signal to 2^{16} or 65536 digital steps; bit depths of 8 or 12 might not be capable of utilising the CCD camera's Dynamic Range in full.

Dark Current - is caused by the generation of thermal electrons in the absence of light in the CCD camera itself; it is a function of exposure time and chip temperature and can be reduced by introducing regulated thermo-electric cooling to provide an operating temperature below 0 °C; dark frame calibration removes the effect of dark current from light frames.

Dynamic Range - is a measure of the difference between the highest and lowest intensities, as well as number of steps in between, which a CCD camera is capable of capturing in a single exposure; to obtain the Dynamic Range, divide Full-Well Capacity by Read Noise.

Frame rate – is the inverse of the time it takes to acquire a frame and read it out.

Frame transfer - exposure is controlled by electronic shutter; exposure and readout occur simultaneously; half of the pixel array is masked and used as a storage area while the other half is unmasked and used to collect the image; once the exposure has ended, the charge is rapidly transferred from the unmasked active imaging area to the masked storage area; readout from the storage area may proceed at a slower pace while the next exposure is being captured; high frame rates are possible but resolution is compromised.

Full frame - an electromechanical shutter is built into the CCD camera; when open, charge is accumulated; when closed, charge is transferred and read out; this provides the highest resolution but limits the frame rate.

Full-Well Capacity / Well Depth - is the number of electrons a pixel can store before it becomes saturated.

Interline - exposure is controlled by electronic shutter; alternating columns of active unmasked imaging area and masked storage area occur enabling rapid transfer from imaging area to storage area in adjacent columns; micro-lenses cover imaging and storage pixels in pairs and direct light to imaging pixels; continuous operation and high frame rates are possible but sensitivity (Quantum Efficiency) is compromised.

Linearity - in CCD cameras with a linear response, the reproduced signal increases in direct proportion to the amplitude of the original source.

Monochrome - black and white CCD cameras have higher sensitivity than colour CCD cameras.

Quantum Efficiency - is a measure of the efficiency with which detected photons are converted to electrons.

Read Noise - is generated by the CCD camera's electronics during ADC and is inherent in the sensor; it is the smallest signal that can be captured.

Appendix A4

Techniques and instruments that are currently employed and which have become the accepted standard to characterise and monitor sites with respect to seeing are compared in Table A4.1 and are as follows: balloon-borne radiosondes, instrumented masts, SHABAR (**SHA**dow **BA**nd **R**anging), LuSci (**Lu**nar **Sci**ntillometer), SCIDAR (**SCI**ntillation **D**etection **A**nd **R**anging), G-SCIDAR (**G**eneralised - **SCIDAR**), HVR-GS (**H**igh **V**ertical **R**esolution **G**-SCIDAR), LOLAS (**LO**w **LA**yer SCIDAR), SLODAR (**SLO**pe **D**etection **A**nd **R**anging), CO-SLIDAR (**CO**upled – **SL**ODAR SC**IDAR**); SODAR (**SO**nic **D**etection **A**nd **R**anging), SNODAR (**S**urface layer **NO**n-**D**oppler **A**coustic **R**adar), DIMM (**D**ifferential **I**mage **M**otion **M**onitor), MASS (**M**ulti-**A**perture **S**cintillation **S**ensor), MASS-DIMM, GSM (**G**eneralized **S**eeing **M**onitor) and PBL (**P**rofileur **B**ord **L**unaire or Lunar Limb Profiler).

Some instruments lend themselves to short intensive seeing campaigns while others are more appropriate to use as long-term seeing monitors on site. In order to determine whether a particular site would present favourable astronomical seeing conditions, a profile of the turbulence strength as a function of altitude, the $C_N^{\ 2}(h)$ profile, at the site is determined. Measurement of the $C_N^{\ 2}(h)$ profile throughout the PBL may be achieved by means of *in situ* measurements making use of sensors mounted on masts, balloons or even aircraft, or by employing remote sensing techniques based on the detection of light, acoustic or radio waves. *In situ* measurements with instrumented balloons provide high-resolution turbulence profiles from surface layer to free atmosphere but the technique is expensive and cannot be used for long-term site monitoring. The remote sensing instruments employed for turbulence and seeing measurements are usually inexpensive and simple to operate. Instruments used for site characterisation campaigns should additionally be as compact and robust as possible. Different remote sensing techniques are sensitive to different layers of the atmosphere and the techniques also differ in the vertical resolution they are able to achieve.

Table A4.1. Comparison of various seeing techniques / instruments (continued on next page).

Technique	Based on	Measured	Calculated	Vertical resolution	Height	Layer	Portability
Mast[1]	Micro-thermal soundings	$D_T(r)$, $C_T^2(h)$, $P(h)$, $T(h)$, $Rh(h)$, $V(h)$	$C_N^2(h)$, r_0, ε_{SL}	Depends on height intervals of sensors	10 – 50 m	Surface	
Balloon[2]	Micro-thermal soundings	$D_T(r)$, $C_T^2(h)$, $P(h)$, $T(h)$, $Rh(h)$, $V(h)$	$C_N^2(h)$ r_0, ε, θ_0, τ_0	5-10 m $V(h)$: 30-50 m	20 m – 30 km	Entire atmosphere excl. surface (0 – 20 m)	
SHABAR[3]/ LuSci[4]	Solar, lunar scintillation	Scintillation	$C_N^2(h)$, r_0, ε_{GL}		~ 100 – 200 m	Ground	Robotic
SCIDAR[5] G-SCIDAR[6] HVR-GS[7] LOLAS[8]	Binary star scintillation	Scintillation	$C_N^2(h)$, $V(h)$, r_0, ε, θ_0, τ_0	~ 200 m ~ 200 m ~ 25 m 12 m	Up to 25 km 0 – 22 km 0 – 1 km 0 – 1 km	Entire atmosphere excl. ground Entire atmosphere Boundary Boundary	$D_{telescope} \geq 1\,\text{m}$ $D_{telescope} \geq 0.4\,\text{m}$
SLODAR[9]	Binary star wave front slope	Wave front slope	$C_N^2(h)$, $V(h)$, r_0, ε	400-700 m 60 m – 150 m	0 – 18 km 0 – 1 km	Entire atmosphere Boundary	$D_{telescope} \geq 1\,\text{m}$ $D_{telescope} = 0.4\,\text{m}$
CO-SLIDAR[10]	Binary star scintillation + wave front slope	Scintillation + wave front slope	$C_N^2(h)$, r_0, ε		20 km	Entire atmosphere	$D_{telescope} \geq 1\,\text{m}$
SODAR[11] SNODAR[12]	Sound pulse backscatter from turbulence	σ_0, $C_T^2(h)$ Doppler shift of scattered pulse	$C_N^2(h)$, $V(h)$	5 m 20 m 0.9 m	0 – 200 m 20 m – 1 km 8 m – 180 m	Ground Boundary Antarctic boundary	Robust, robotic
DIMM[13]	Differential image motion in twin images of star	Differential image motion variance - σ_l, σ_t	r_0, ε, σ_I^2, θ_0, τ_0	Integrated ε	Entire atmosphere	Entire atmosphere	$D_{telescope} = 8" - 14"$ Compact, robust, robotic, site monitoring

Table A4.1. Comparison of various seeing techniques / instruments (continued from previous page).

Technique	Based on	Measured	Calculated	Vertical resolution	Height	Layer	Portability
MASS[14]	Scintillation of light from single star	Intensity fluctuations, scintillation indices	σ_I^2 fit to model provides $C_N^2(h)$, r_0, ε_{FA}, θ_0, τ_0	500 m Limited to six turbulent layers at 0.5, 1, 2, 4, 8 and 16 km in fixed-layer model	Entire atmosphere	Entire armosphere excl. ground (<0.5 km) - only free atmosphere seeing	$D_{telescope} = 8" - 14"$ Compact, robust, robotic, continuous site monitoring
MASS-DIMM[15]	Combination of MASS & DIMM	Scintillation indices, differential image motion variance	$C_N^2(h)$, r_0, ε, θ_0, τ_0, σ_I^2	MASS: 500 m DIMM: integrated ε	MASS: entire atmosphere excl. ground DIMM: entire atmosphere	Entire atmosphere + ground-layer seeing from DIMM – MASS: $\varepsilon_{BL} = \left(\varepsilon_{DIMM}^{5/3} - \varepsilon_{MASS}^{5/3}\right)^{3/5}$	Compact, robust, robotic, continuous site monitoring
GSM[16]	Single star Angle of Arrival (AA) fluctuations + scintillation	AA spatio-temporal correlations σ_I^2	ε, $\mathcal{L}_0$, σ_I^2, θ_0, τ_0, $V(h)$				4+ Maksutov telescopes each with $D_{telescope} = 10$ cm
PBL[17]	DIMM of point along lower lunar limb	Differential image motion variance	$C_N^2(h)$, $\mathcal{L}_0(h)$, θ_0, r_0, ε (15+ layers)	High ε for 15+ layers	Entire atmosphere	Entire atmosphere	$D_{telescope} = 16"$ (portable version)

1 Echevarría (1998 & 2003); Sánchez (2003)
2 Bufton et al. (1972) ; Barletti et al. (1977) ; Azouit et al. (1980) ; Vernin & Muñoz-Tuñón (1992) ; Azouit & Vernin (2005)
3 Beckers (1993 & 2001); Moore et al. (2006); Sliepen et al. (2010)
4 Tokovinin (2007); Tokovinin, Bustos & Berdja (2010)
5 Vernin & Roddier (1973); Rocca et al. (1974)
6 Avila et al. (1997); Fuchs et al. (1998)
7 Egner et al. (2006); Egner & Masciadri (2007)
8 Avila et al. (2008)
9 Wilson (2002 & 2010); Wilson, Butterley & Sarazin (2009); Osborn et al. (2010)
10 Védrenne et al. (2007) ; Robert et al. (2009 & 2011)
11 Crescenti (1997)
12 Lawrence et al. (2007) ; Bonner et al. (2008, 2009 & 2010)
13 Sarazin & Roddier (1990); Vernin & Muñoz-Tuñón (1995)
14 Kornilov et al. (2003) & Tokovinin et al. (2003)
15 Kornilov et al. (2007)
16 Martin et al. (1994); Conan et al. (1999a & 1999b); Ziad et al. (2000)
17 Ziad et al. (2010)

$D_T(r)$: temperature structure function

$C_T^2(h)$, $C_N^2(h)$: temperature and refractive index structure parameters

$P(h)$, $T(h)$, $Rh(h)$, $V(h)$: pressure, temperature, relative humidity, wind profiles

r_0 : Fried parameter

ε, ε_{SL}, ε_{GL} : total, surface layer, ground layer seeing

θ_0 : isoplanatic angle

τ_0 : coherence time

σ_0 : backscatter cross-section

σ_l, σ_t : longitudinal, transverse variation of differential image motion

σ_I^2 : scintillation index

$\mathcal{L}_0(h)$: outer scale of turbulence

Some instruments provide turbulence profiles from ground level to the top of the atmosphere, the so-called vertical turbulence profilers, which are able to provide the vertical distribution of $C_N{}^2(h)$, wind speed as well as the outer scale of turbulence. In contrast, the integrated turbulence monitors are only able to provide integrated values for the seeing. Remote sensing techniques generally also provide the classical Fried parameter and the seeing as well as other seeing parameters such as the isoplanatic angle, coherence time and outer scale of turbulence.

Instrumentation, such as the DIMM, MASS, MASS-DIMM, GSM and PBL, that could become available for use during short seeing campaigns, are described in detail below, as is the necessity of co-locating an AWS and cloud mapper with any on-site seeing monitor:

DIMM

The following discussion of the DIMM instrument is based on descriptions by Sarazin and Roddier (1990) as well as by Vernin and Muñoz-Tuñón (1995):

The DIMM has become the standard instrument for characterising sites with respect to astronomical seeing. It does so by estimating the integrated seeing over the entire atmosphere in the column of air above the telescope. DIMM measures differential image motion variance caused by atmospheric turbulence in two images (two columns of light) taken of the same star at exactly the same moment. Seeing is then related to this variance of differential image motion through use of the Fried parameter. A DIMM is usually a robust set-up, which allows for transportation over rough terrain during site testing campaigns. It consists of a telescope, mount and CCD camera. The telescopes used are commercially available SCTs with apertures ranging from 8" to 14". CCD cameras are inexpensive, off-the-shelf cameras able to provide a fast frame-rate and preferably offering an adjustable electronic shutter. A high-quality equatorial mount and auto-guiding are required for accurate pointing and tracking. A PC and the appropriate software allow for robotic control of the entire system. The telescope entrance pupil is covered by an aperture mask. Oftentimes the telescope's dust cover will have been modified to provide this mask. The mask has two circular sub-apertures cut into it. The sub-apertures vary in diameter

from ~ 5-11 cm and are separated by a distance of a few times the sub-aperture diameter, ~ 14-25 cm, depending on the telescope aperture diameter. A wedge prism is placed in one of the sub-apertures. It displaces the light coming through the sub-aperture. Well-separated twin images of the same star are thus detected by the CCD camera. A beam splitter could also be used to obtain such twin images.

A bright star, less than 30° from zenith, is observed for a few hours while it crosses the meridian. Each sub-aperture observes the star through a different column of air. A wedge prism on one of the sub-apertures allows a second image of the star to be formed by reflection of the light cone going through that sub-aperture. The two star images are

Figure A4.1. DIMM mask with wedge prism (source: Andrei Tokovinin).

detected by the CCD camera, which takes a set of ~ 200-400 short-exposure (~ 2-5 ms) images required to capture the rapid image motion. The variances in differential motions of the two image centroids are measured in directions longitudinal (parallel) and transverse (perpendicular) to the line connecting the centres of the two sub-apertures. Two independent values for the Fried parameter (r_0) are estimated - one related to the variance in longitudinal differential motion (σ_l), the other to the variance in transverse differential motion (σ_t). These two Fried parameter values should be the same but strong winds and finite exposure time will cause them to differ. Seeing (ε) is obtained from the Fried parameter values. Seeing estimates are referred to zenith and corrected for air mass, system noise and statistical errors. Two windows, each containing one of the image centroids, are displayed on-screen, as is the seeing value, FWHM, flux and scintillation index. Seeing

estimations are provided approximately every minute. Guiding takes place between 1-minute data accumulations. The differential technique allows distinguishing between image motion caused by turbulence and that caused by telescope vibrations and tracking errors. DIMM systems have become reliable, cost-effective, portable, easy to set up, operate and maintain and are now well-documented and easy to duplicate. DIMM systems can operate in robotic mode with all functions controlled by computer.

MASS

The MASS instrument is described in accordance with details provided in Kornilov *et al.* (2003) and Tokovinin *et al.* (2003):

MASS is a standard instrument for determining low-resolution atmospheric turbulence profiles above sites. Scintillation (or twinkling) of star light is caused by atmospheric turbulence. Scintillation from the light of a single star is measured in four concentric annular apertures in the image pupil plane. Intensity fluctuations in the four apertures are statistically analysed to provide scintillation indices (SIs). The indices are fitted to a turbulence-layer model and the turbulence profile $C_N^2(h)$ is recovered. MASS is a small, robust instrument fed by a SCT setup with auto-guiding similar to the DIMM setup. A small detector box contains the optics (including a segmentator), photo-multiplier tubes (PMTs) and electronics. The segmentator consists of a circular mirror surrounded by three concentric, reflective rings with varying tilts. It separates the image of the telescope exit pupil into four concentric-ring apertures A, B, C and D with inner and outer diameters ranging from 2 cm (A) to 13 cm (D), respectively. Scintillations are detected in the four concentric-ring apertures by the PMTs operating in photon-counting mode. The control software, Turbina, runs under Linux and controls the instrument through a graphical user interface (GUI) and provides real-time data reduction and automatic operation. A single bright star within 45° of zenith is observed. The flux from the star is spatially filtered by the four concentric-ring apertures. The varying aperture diameters allows for turbulent layers causing the scintillation to be identified and their contribution to the scintillation to be found. Light from each aperture is detected by four PMTs sampling at 1 ms in photon-counting mode. Turbina processes the photon counts and calculates SIs for each aperture every second. SIs for each aperture as well as each aperture pairing are calculated,

delivering four normal and six differential SIs. By knowing the weighting functions (WFs), which represent layer-contributions to SIs, and the SIs themselves, and by fitting these indices to a simple model with a small number of layers, a low vertical resolution (500 m) turbulence profile $C_N{}^2(h)$ is obtained. The fixed-layer model provides for six thin turbulent layers at 0.5, 1, 2, 4, 8 and 16 km altitude. The floating-layer model provides for three layers located at any altitude. Every minute, average indices are computed and turbulence parameters determined. The Fried parameter (and therefore the seeing) is related to the integral of $C_N{}^2(h)$ over the whole atmosphere. Near-ground turbulence does not produce any scintillation. MASS is therefore not sensitive to ground-layer turbulence (< 0.5 km). Only free-atmosphere seeing is estimated. The isoplanatic angle (θ_0) is also derived from the turbulence profile. Turbina displays the turbulence evolution on-screen in real time. The MASS has become a simple and inexpensive instrument and can be used as a turbulence profiler for continuous site monitoring.

MASS-DIMM

Kornilov *et al.* (2007) provides the basis for the following discussion of the combined MASS-DIMM instrument:

Ground-layer turbulence is not sensed by MASS as it does not produce any scintillation, whilst DIMM measures the seeing in the atmosphere as a whole. Combining MASS and DIMM, the seeing in the lowest 500 m can be found by subtracting the turbulence integral measured with MASS (free atmosphere seeing) from that measured with DIMM (total integrated seeing). The MASS-DIMM instrument uses the same telescope and observes the same star thereby sensing the same turbulent volume.

The SALT MASS-DIMM instrument is attached to a 10" LX200GPS Meade SCT, the same telescope feeding both MASS and DIMM channels. The telescope is mounted on an Astro-Physics 900 GTO equatorial mount mated to a sturdy pier at ground level. A Grasshopper Pixelfly CCD camera with fast frame-rate capable of taking short exposures is attached to the DIMM channel. DIMM data is processed with TimDIMM software, MASS data with Turbina 2.06 software. The system is controlled by Python script running on a

Mac mini. The MASS-DIMM instrument consists of a small detector box which houses common optics and electronics. Electronics consist of the PMTs, their high-voltage supply, photon counters and microprocessors. The light is split into a MASS channel and a DIMM channel by a pupil plate

Figure A4.2. The SALT MASS-DIMM in operation at the SAAO site in Sutherland with the MASS-DIMM instrument attached at the exit pupil displayed in insert bottom right.

assembly. The light is further separated into four MASS sub-channels by a segmentator and directed to the four PMTs. Two mirrors provide two DIMM sub-channels which direct the light to the CCD camera for detecting the two image centroids of the same star. A single bright star within 30° from zenith is acquired. The DIMM channel is used to centre and guide on the star. TimDIMM and Turbina software are started and seeing measurements made in both DIMM and MASS channels with 1-minute integration time. Measurements are terminated and a new target is acquired once the star moves outside of 30° from zenith. As described in the section above, DIMM measures the differential image motion of the star in the two DIMM sub-channels while MASS measures the scintillation of the same star in the four MASS sub-channels (corresponding to different turbulent layers in the atmosphere). The Fried parameter and thus seeing is estimated from the differential motion measured by the DIMM channel. The DIMM channel delivers total

integrated seeing (Fried parameter) for all layers, from the ground layer up to the free atmosphere, i.e. seeing in the entire atmosphere. From the scintillation indices measured by the MASS channel, a low-resolution turbulence profile is constructed, and seeing from 500 m above the telescope to the top of the atmosphere can be estimated. Ground-layer seeing can thus be determined from the difference between the seeing obtained from DIMM and that obtained from MASS.

The MASS-DIMM instrument is fast becoming the standard seeing monitor to be found at astronomical observatories. It is compact, robust, simple to use and relatively inexpensive and can be fully automated for continuous turbulence monitoring at a site.

GSM

The following discussion of the GSM instrument refers to descriptions in Martin *et al.* (1994), Conan *et al.* (1999a and 1999b) and Ziad *et al.* (2000):

The GSM measures the angle of arrival (AA) fluctuations at different points on the wave front and computes AA spatio-temporal correlations from which the seeing (ε), outer scale of turbulence ($\mathcal{L}_0$), isoplanatic angle (θ_0) and coherence time for the AA fluctuations (τ_0) may be deduced. It consists of several, usually four (providing six baselines), 10-cm aperture diameter Maksutov telescopes installed on equatorial mounts on piers set up in an L-shaped configuration to improve sensitivity to the outer scale. Accompanying each telescope is a detection module housing, optical and detector components. All telescopes observe the same single bright star at zenith angles between 0° and 45°. AA fluctuations are measured by flux modulation (produced by the displacement of the star image over a Ronchi grating) and the transmitted flux is detected by photomultiplier. AA covariances of the AA fluctuations for the various baselines are computed. Two of the telescopes share a mount and pier, operating as a DIMM and measures the AA differential variances from which the seeing (ε) is obtained. The outer scale ($\mathcal{L}_0$) is obtained from the ratio of AA covariances to differential variances. The recorded flux provides the scintillation index (σ_I^2) from which the isoplanatic angle (θ_0)

may be deduced. Wind speed of the turbulent layers is extracted from AA spatio-temporal correlations from which the wave front constant time (τ_0) is deduced.

During the Sutherland campaign, two Maksutov 10-cm aperture diameter telescopes, each with a detection module containing optics and PMT detectors, were set up in a binocular configuration. The GSM modules were mounted on an Astro-Physics 900 GTO equatorial mount mated to a rigid pier at ground level. A single star with magnitude < 3 and within 30° of zenith was observed through both apertures. For each of the modules, a diaphragm filtered out noise from the sky background, the light was aligned by a collimator and directed to an oscillating mirror, which deflected it onto the Ronchi grating and, on passing through the grating, was detected by the PMTs. Without turbulence present, light would produce a regular sine wave as it passes through the grating. With turbulence present, the phase of the sine wave is shifted. From the phase difference, the seeing, isoplanatic angle and outer scale of turbulence were deduced.

Figure A4.3. The GSM at Sutherland operated in DIMM mode with the two Maksutov telescopes sharing the same mount.

PBL

The PBL instrument is discussed with reference to Ziad *et al*. (2010):

The PBL is a new instrument capable of extracting both $C_N^2(h)$ and $\mathcal{L}_0(h)$ with high vertical resolution. A portable version of the PBL was used for the first time during the Sutherland seeing campaign. The PBL observes the lunar limb using the DIMM method. Equipment consists of a Meade 16M SCT mounted on an Astro-Physics 1200 GTO equatorial mount mated to a sturdy pier. The front aperture of the telescope is covered by a mask with two 6-cm diameter sub-apertures separated by ~ 30 cm. The imaging module contains the optics and a PixelFly CCD camera, which are all mounted on a micro-control plate for adjustment with software.

Figure A4.4. The PBL setup at Sutherland with SALT in the background.
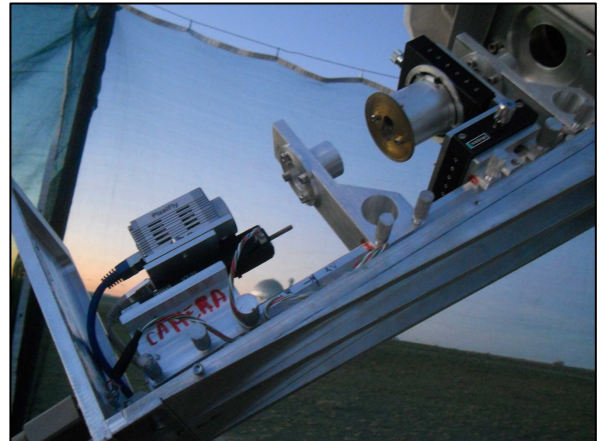

Figure A4.5. The PBL's optical module includes a PixelFly CCD camera.

The CCD camera has an imaging frequency of 33 Hz and its exposure time is set to 1 or 2 ms to freeze image motion. The two sub-apertures in the mask provide two images of the Moon's limb. A Dove prism is used to reverse one of the two images to prevent bright parts from overlapping. Two mirror images of the Moon's lower limb are thus obtained. The two sub-apertures observe the same points along the Moon's limb. Wave fronts arrive at the two sub-apertures from two directions separated by and angle θ. The Moon's limb provides a continuum of point sources with varying angular separation. The PBL measures the differential image motion of all these points along the Moon's limb. The $C_N^2(h)$ profile is retrieved by analysing the angular correlation of the differential distance between

the two lunar edges. The PBL is also capable of providing the outer scale profile, isoplanatic angle and the contribution to the seeing of 15+ layers. As with the DIMM method, the use of differential image motion compensates for telescope vibrations and tracking errors.

Weather station and cloud mapper

A site's atmospheric stability is dependent on minimal variation in air temperature and atmospheric pressure, on low relative humidity, precipitable water vapour, precipitation and wind speed as well as on a high frequency of clear-sky conditions. Knowledge of these parameters' diurnal and seasonal distribution is necessary to fully characterise a site with respect to meteorological and turbulence conditions and to determine the number of usable nights (or days) for observing. Basic weather data such as temperature, pressure, humidity, precipitation, wind speed and direction as well as cloud cover can be obtained from weather services, weather satellite data and climate diagnostic archives, which also make long-term meteorological records available, but temporal and spatial resolution may be poor. It is therefore necessary to have an Automatic Weather Station (AWS) installed at a site for continuous monitoring of local meteorological parameters in order to obtain both instantaneous and long-term records of meteorological data thereby establishing a baseline of basic on-site weather data. AWSs such as systems by Davis Instruments and Campbell Scientific Instruments are able to provide reliable measurement of air and soil temperature, barometric pressure, relative humidity, precipitation, wind speed and direction and solar radiation. Data are automatically recorded to a data logger module. A solar panel can be used to charge the 12-volt battery the data logger is connected to. Such an AWS should be installed in close proximity to the telescope. Instruments such as the Boltwood Cloud Sensor and the SBIG All Sky Camera can be installed to monitor cloud cover. The Boltwood cloud sensor detects clouds in and indirect manner – it senses infrared radiation from the sky to determine the sky temperature, compares it to the ambient temperature and reports clear sky conditions if the sky temperature is at least 20°C colder than the ambient temperature. The Boltwood Cloud Sensor also provides the temperature, humidity, dew point and is able to sense wetness and detect daylight. The SBIG All Sky Camera makes use of an SBIG ST237 CCD and a fisheye lens to capture images of the entire sky.

Figure A4.6. The Boltwood
Cloud Sensor at HartRAO.

Figure A4.7. The SAAO All Sky Camera at
Sutherland is located together with the
SALT MASS-DIMM in the ox wagon
enclosure.